The Astrophysical Journal Supplement Series, 142:269–283, 2002 October


# ANALYTICAL APPROXIMATIONS TO HYDROSTATIC SOLUTIONS AND SCALING LAWS OF CORONAL LOOPS

Markus J. Aschwanden and Carolus J. Schrijver
Lockheed Martin Advanced Technology Center, Solar and Astrophysics Laboratory, Department L9-41,
Building 252, 3251 Hanover Street, Palo Alto, CA 94304; aschwanden@lmsal.com
*Received 2002 February 14; accepted 2002 May 22*

## ABSTRACT

We derive accurate analytical approximations to hydrostatic solutions of coronal loop atmospheres, applicable to uniform and nonuniform heating in a large parameter space. The hydrostatic solutions of the temperature $T(s)$, density $n_e(s)$, and pressure profile $p(s)$ as a function of the loop coordinate $s$ are explicitly expressed in terms of three independent parameters: the loop half-length $L$, the heating scale length $s_H$, and either the loop-top temperature $T_{\max}$ or the base heating rate $E_{H0}$. The analytical functions match the numerical solutions with a relative accuracy of $\lesssim 10^{-2}$–$10^{-3}$. The absolute accuracy of the scaling laws for loop base pressure $p_0(L, s_H, T_{\max})$ and base heating rate $E_{H0}(L, s_H, T_{\max})$, previously derived for uniform heating by Rosner et al., and for nonuniform heating by Serio et al., is improved to a level of a few percent. We generalize also our analytical approximations for tilted loop planes (equivalent to reduced surface gravity) and for loops with varying cross sections. There are many applications for such analytical approximations: (1) the improved scaling laws speed up the convergence of numeric hydrostatic codes as they start from better initial values, (2) the multitemperature structure of coronal loops can be modeled with multithread concepts, (3) line-of-sight integrated fluxes in the inhomogeneous corona can be modeled with proper correction of the hydrostatic weighting bias, (4) the coronal heating function can be determined by forward-fitting of soft X-ray and EUV fluxes, or (5) global differential emission measure distributions $dEM/dT$ of solar and stellar coronae can be simulated for a variety of heating functions.

*Subject headings:* hydrodynamics — stars: coronae — Sun: corona

## 1. INTRODUCTION

Accurate density and temperature models are fundamental tools to explore the physical processes of plasma heating and cooling in solar and stellar coronae. The tremendous increase of imaging data in soft X-rays and extreme ultraviolet (EUV) produced by the *Yohkoh, SoHO, TRACE, ROSAT, ASCA, Chandra*, and *Newton* spacecraft have stimulated modeling efforts in an unprecedented way. The modeling of coronal loops with hydrostatic solutions, which ensure the basic physical conservation laws of mass, momentum, and energy, however, is computation-expensive with numeric codes, particularly for large sets to model entire stellar coronae. Therefore, appropriate analytical expressions for their density and temperature profiles are highly desirable. At this time, no analytical solutions are known for the hydrostatic equations, except for an approximate temperature function in the special case of uniform heating, constant cross section, and zero gravity (Rosner, Tucker, & Vaiana 1978; Kuin & Martens 1982). In this study we use a numerical code to compute some 1000 hydrostatic solutions in a large parameter space, for uniform as well as for nonuniform heating functions, and develop accurate analytical approximations by fitting them to the numerical solutions. By the same token, we quantify also the well-known scaling laws of loop base pressure and heating rate as derived earlier by Rosner et al. (1978) and Serio et al. (1981), but with higher precision, and add loop expansion as a parameter. The new analytical formulation consists of explicit expressions as a function of five independent parameters and can conveniently be applied to forward-fitting of coronal data and statistical studies of solar and stellar atmospheres (e.g., Schrijver & Aschwanden 2002).

The content of the paper includes a definition of the hydrodynamic equations as they are used here (§ 2), a brief description of a numerical code that is used to calculate the exact hydrostatic solutions (§ 3), the derivation of analytical approximations and more accurate scaling laws (§ 4), generalizations for very short heating scale lengths, inclined loops, and loops expanding with height (§ 5), and a discussion of applications (§ 6).

## 2. HYDRODYNAMIC EQUATIONS

We define the quantities of the time-independent hydrodynamic equations used in this study, which have been used with slightly different notations, approximations, assumptions, and degree of completeness in previous work (e.g., Parker 1958; Rosner et al. 1978; Priest 1982; Mariska et al. 1982; Craig & McClymont 1986; Klimchuk, Antiochos, & Mariska 1987; Klimchuk & Mariska 1988; Withbroe 1988; Bray et al. 1991).

The one-dimensional, time-independent ($d/dt = 0$) hydrodynamic equations involve the equations of mass conservation,

$$\frac{1}{A}\frac{d}{ds}(nvA) = 0 \ , \tag{1}$$

the momentum equation,

$$mnv\frac{dv}{ds} = -\frac{dp}{ds} + \frac{dp_{\rm grav}}{dr}\left(\frac{dr}{ds}\right) \ , \tag{2}$$

and the energy equation (expressed in conservative form),

$$\frac{1}{A}\frac{d}{ds}(nvA[\epsilon_{\rm enth}+\epsilon_{\rm kin}+\epsilon_{\rm grav}]+AF_C)=E_H+E_R\ , \quad (3)$$

where $s$ is the distance along the loop measured from the solar surface, $r$ is the radial distance to Sun center, $A(s)$ is the loop cross section, $m$ is the average particle mass, $n(s)$ is the particle density, $v(s)$ is the velocity of a single fluid, $p(s)$ is the gas pressure, $p_{\rm grav}(r)$ is the gravitational pressure, $\epsilon_{\rm enth}(s)$ is the enthalpy, $\epsilon_{\rm kin}(s)$ is the kinetic energy, $\epsilon_{\rm grav}(r)$ is the gravitational potential, $F_C(s)$ is the conductive flux, $E_H(s)$ is the volumetric heating rate, and $E_R(s)$ is the volumetric radiative loss rate.

The mass density (also called $\rho = mn$) of a fully ionized gas is defined by

$$mn(s)=m_e n_e(s)+m_i n_i(s)\approx \mu m_p n_e(s)\ , \quad (4)$$

with $m_i=\mu m_p$ the average ion mass (i.e., $\mu\approx(10\times 1+1\times 4)/11=1.3$ for a coronal composition of H : He = 10 : 1), $m_p=1.67\times 10^{-24}$ g the proton mass, and the density $n(s)$ is assumed to be equal for electrons and ions ($n=n_e=n_i$) in a fully ionized gas.

The total pressure $p(s)$ of a fully ionized gas is defined by the ideal gas law and relates to the (electron) density $n(s)$ by

$$p(s)=[n_e(s)+n_i(s)]k_{\rm B}T(s)\approx 2n(s)k_{\rm B}T(s)\ , \quad (5)$$

where $k_{\rm B}=1.38\times 10^{-16}$ erg K$^{-1}$ is the Boltzmann constant and $T(s)$ is the electron temperature.

The enthalpy energy $\epsilon_{\rm enth}(s)$ comprises the heat energy acquired (or lost) at constant volume, plus the work done against the pressure force when the volume changes, and is defined by

$$\epsilon_{\rm enth}(s)=\tfrac{5}{2}k_{\rm B}T(s)\ , \quad (6)$$

the kinetic energy $\epsilon_{\rm kin}(s)$ is

$$\epsilon_{\rm kin}(s)=\tfrac{1}{2}mv^2(s)\ , \quad (7)$$

the gravitational potential $\epsilon_{\rm grav}(r)$ is

$$\epsilon_{\rm grav}(r)=-\frac{GM_\odot m}{r}=-mg_\odot\left(\frac{R_\odot^2}{r}\right)\ , \quad (8)$$

with the solar gravitation $g_\odot=GM_\odot/R_\odot^2=2.74\times 10^4$ cm s$^{-2}$ and solar radius $R_\odot=6.96\times 10^{10}$ cm. The differential gravitational pressure, used in the momentum equation (2), is

$$\frac{dp_{\rm grav}}{dr}(r)=-\frac{GM_\odot mn}{r^2}=-mng_\odot\left(\frac{R_\odot^2}{r^2}\right)\ . \quad (9)$$

The next term of the energy balance equation describes the divergence of the conductive flux, which in a one-dimensional flux tube model is

$$F_C(s)=\left[-\kappa T^{5/2}(s)\frac{dT(s)}{ds}\right]=-\frac{2}{7}\kappa\frac{d}{ds}\left[T^{7/2}(s)\right]\ , \quad (10)$$

with $\kappa=9.2\times 10^{-7}$ erg s$^{-1}$ cm$^{-1}$ K$^{-7/2}$ the Spitzer conductivity.

The most unknown term is the volumetric heating rate $E_H(s)$ along the loop, which crucially depends on assumptions on the physical heating mechanism. Many previous loop models assumed uniform heating, $E_H(s)=$ const (e.g., Rosner et al. 1978), for sake of simplicity. Here we parameterize the heating function with two parameters: with the base heating rate $E_{H0}$ and an exponential scale length $s_H$, as it was introduced by Serio et al. (1981),

$$E_H(s)=E_0\exp\left(-\frac{s}{s_H}\right)=E_{H0}\exp\left(-\frac{s-s_0}{s_H}\right)\ . \quad (11)$$

While Serio's base heating rate $E_0$ refers to the photosphere (at $s=0$), we introduce a base heating rate $E_{H0}$ that refers to the same reference height $s=s_0$ as we will refer the base temperature $T_0$, the base pressure $p_0$, and the base density $n_0$. This *Ansatz* allows us to model nonuniform heating localized above the loop footpoints from arbitrary small heating scale lengths ($s_H\ll L$) up to the limit of uniform heating ($s_H\gg L$). Alternative parameterizations of heating functions that are suitable for loop-top heating have been used elsewhere (e.g., Priest et al. 2000; MacKay et al. 2000).

The radiative losses $E_R(s)$ are proportional to the square of the electron density, $n_e^2(s)$, multiplied with a temperature-dependent function $\Lambda(T)$ (Tucker & Koren 1971),

$$E_R(s)=-n_e^2(s)\Lambda[T(s)]\ , \quad (12)$$

which was approximated by Rosner et al. (1978) by piecewise power laws [see Appendix A in Rosner et al. 1978 for the definition of $\Lambda(T)$]. For a discussion of other calculations of the radiative loss function and consequences on the hydrostatic solutions see § 4.5.

The one-dimensional parameterization of loops with a distance coordinate $s$ involves an angle $\phi(s)$ between the magnetic field line (defining a loop) and the radial direction $r$. The simplest geometry employs semicircular loops, for which the height $h(s)$ in the loop plane relates to the loop distance $s$ by

$$h(s)=r(s)-R_\odot=\frac{2L}{\pi}\sin\left(\frac{\pi s}{2L}\right)\ , \quad (13)$$

with $L$ the loop half-length. The derivative $(dh/ds)$ defines then the cosine of the angle $\phi$ used in the momentum balance equation (2),

$$\left(\frac{dr}{ds}\right)=\left(\frac{dh}{ds}\right)=\cos\left(\frac{\pi s}{2L}\right)=\cos\phi\ . \quad (14)$$

For the variation of the loop cross section $A(s)$ along the loop coordinate $s$ we follow the line-dipole model of Vesecky, Antiochos, & Underwood (1979). In their model the inner and outer field line of a loop intersect in the lowest subphotospheric point, where the line dipole is buried, while the cross section varies as a $\sin^2$ function, expanding by a factor of $\Gamma$ from the photosphere to the loop apex. Because we are using a semicircular geometry for the loops, only loops with an expansion factor of $\Gamma=2$ can be accommodated in the geometry of Vesecky et al. (1979). To allow for an arbitrary large range of expansion factors $\Gamma$ in semicircular loops we generalize the model of Vesecky et al. (1979) by relaxing the condition of a zero cross section at the subphotospheric anti-apex point ($s=-L$). We define a generalized cross section function

$$A(s)=A_0\Gamma\sin^2\left(\frac{\pi}{2}\frac{s+s_{\rm sub}}{L+s_{\rm sub}}\right)\ , \quad (15)$$

where the zero cross section point is located at position

$s = -s_{\rm sub}$ and depends on the expansion factor $\Gamma$ as

$$s_{\rm sub}(\Gamma) = \frac{L}{[(\pi/2)/\arcsin(1/\Gamma^{1/2}) - 1]} \ . \qquad (16)$$

This definition yields a zero cross section at location $s = -s_{\rm sub}$, i.e., $A(s = -s_{\rm sub}) = 0$, a reference cross section $A_0$ at the photosphere, i.e., $A(s = 0) = A_0$, and an expanded cross section by a factor $\Gamma$ at the loop apex, $A(s = L) = A_0\Gamma$.

## 3. NUMERIC CODE

Solving the hydrodynamic equations means to find functions $T(s)$ and $n(s)$ that fulfil the momentum and energy balance for every position $s$ along a loop (with half-length $L$) in the range of $s_0 < s < L$ and that match the prescribed boundary conditions: i.e., the temperature at the footpoint, $T(s = s_0) = T_0$, and at the loop-top, $T(s = L) = T_{\rm max}$, and the requirement of vanishing conductive flux at the boundaries, $F_C(s = s_0) = 0$ and $F_C(s = L) = 0$. The latter requirement enables symmetric loop solutions and prevents energy transfer across the boundaries.

We developed an explicit code for time-independent solutions ($d/dt = 0$) and no flows, $v(s) = 0$, but for a variable cross section $A(s)$ (eqs. [15] and [16]). In order to resolve the steep temperature gradient in the transition region, we use a logarithmic grid for the spatial coordinate $s_i, i = 0, \ldots, n$. The initial boundary conditions at $s_0$ are specified by the minimum temperature $T_0$, the base pressure $p_0$, and base heating rate $E_{H0}$. In a half-loop with half-length $L$ we step from the footpoint to the loop-top along the one-dimensional loop coordinate $s_i$, calculating iteratively $E_H(s_i)$, $T(s_i)$, $\lambda_p(s_i)$, $p(s_i)$, $n(s_i)$, $E_R(s_i)$.

A defining parameter set for a unique solution includes the base heating rate $E_{H0}$, the heating scale length $s_H$, the loop half-length $L$, the base pressure $p_0$, and the base temperature $T_0$ at base position $s_0$. We choose a transition region temperature of $T_0 = 2 \times 10^4$ K and height of $s_0 = 1.3$ Mm like in other studies. An iteration starting with these boundaries will yield a particular loop-top temperature $T(s = L) = T_{\rm max}$ and a generally not-vanishing conductive flux $F_C(s = L)$ at the loop-top. We iterate the starting values of the heating rate $E_{H0}$ and base pressure $p_0$ until (i) a vanishing conductive flux at the loop top $F_C(s = L) = 0$, and (ii) a desired loop-top temperature $T_{\rm max}$ is obtained. The number of iterations is drastically reduced by using the approximate solutions of the scaling laws found from previous runs. For the stepping along the loop coordinate $s_i$ it turned out that linear steps $\Delta s_i = s_{i+1} - s_i = {\rm const}$ are not sufficiently accurate to resolve the steep temperature gradient in the transition region. Therefore, we used a logarithmic grid with the highest resolution near at the loop base $s = s_0$.

An example of a numeric solution is shown in Figure 1, for the case of a uniformly heated loop ($s_H \gg L$) with a half-length of $L = 40$ Mm and loop-top temperature $T_{\rm max} = 1.0$ MK. The solutions of the temperature $T(s)$, density $n(s)$, and pressure profile $p(s)$ are shown in a linear display (left row), in a logarithmic display (middle row), in order to demonstrate how the transition region is resolved with the numeric code. The conductive flux $F_C(s)$, the momentum balance, and the energy balance are shown in the panels on the right-hand side of Figure 1. Correct numeric solutions are verified a posteriori by calculating the momentum and energy balance from the solutions of $T(s)$, $n(s)$, and $p(s)$ with equations (2) and (3), which should yield a zero value for all steps $s$ (Fig. 1, *thick lines*).

We compute some 1000 hydrostatic solutions in a three-dimensional parameter space, for 20 logarithmically distributed loop lengths between $L = 4$ Mm and $L = 400$ Mm, for 20 logarithmically distributed heating scale lengths between $s_H = 4$ Mm and $s_H = 400$ Mm, and for four temperatures $T_{\rm max} = 1$, 3, 5, and 10 MK, excluding cases that gravitationally are not stably stratified ($s_H/L \lesssim 0.3$, see Serio et al. 1981 and Aschwanden, Schrijver, & Alexander 2001). The subset of hydrostatic solutions with a loop-top temperature of $T_{\rm max} = 1$ MK is identical with the solutions calculated in a previous study (Aschwanden et al. 2001), where a similar explicit algorithm was used (with start from the loop-top boundary and stepping downward), but had the disadvantage that the footpoint boundaries could not always be met with high precision. The new code described here resolves the transition region much better and thus yields more accurate solutions, matching both boundary conditions with equal precision. We used a standard resolution of $n = 200$ points, logarithmically distributed along the loop, for which our explicit solving scheme turned out to be sufficiently accurate. These numerically computed hydrostatic solutions build the basis for the following derivation of analytical approximations and tests of the accuracy of previously published loop scaling laws.

## 4. ANALYTICAL APPROXIMATIONS

The hydrostatic equations cannot be solved analytically, because the momentum (eq. [2]) and energy equation (eq. [3]) represent a coupled equation system, where the energy equation (eq. [3]) is a second-order nonlinear ordinary differential equation. We thus strive for useful analytical approximations.

### 4.1. *Temperature Function $T(s)$*

The temperature function is involved with a second-order derivative in the conductive loss term. An analytical expression has been derived for the inverse temperature function $s(T)$ for the special case of constant pressure, $p(s) = {\rm const}$, uniform heating, $E_H(s) = {\rm const}$, constant cross section, and no gravity, by Rosner et al. (1978, eq. [C1] therein), which we will use for comparison:

$$s(T) = s(T_0) + 2.5 \times 10^5 p_0^{-1} \times \left(9.6 \times 10^{-16} T_{\rm max}^3 \{\arcsin(T/T_{\rm max}) - (T/T_{\rm max})[1 - (T/T_{\rm max})^2]^{1/2}\} + 1\right) . \qquad (17)$$

Another analytical approximation was derived by Martens (1981), given also in Kuin & Martens (1982) or Martens, Kankelborg, & Berger (2000), characterized by the incomplete $\beta$ function and the complete $\beta$ function (B), in explicit form for the temperature,

$$T(s) = T_{\rm max}\left(\beta^{-1}\left\{\left(\frac{z}{L}\right)B\left[\frac{11+2\gamma}{4(2+\gamma)}, 0.5\right]; \frac{11+2\gamma}{4(2+\gamma)}, 0.5\right\}\right)^{1/(2+\gamma)} , \qquad (18)$$

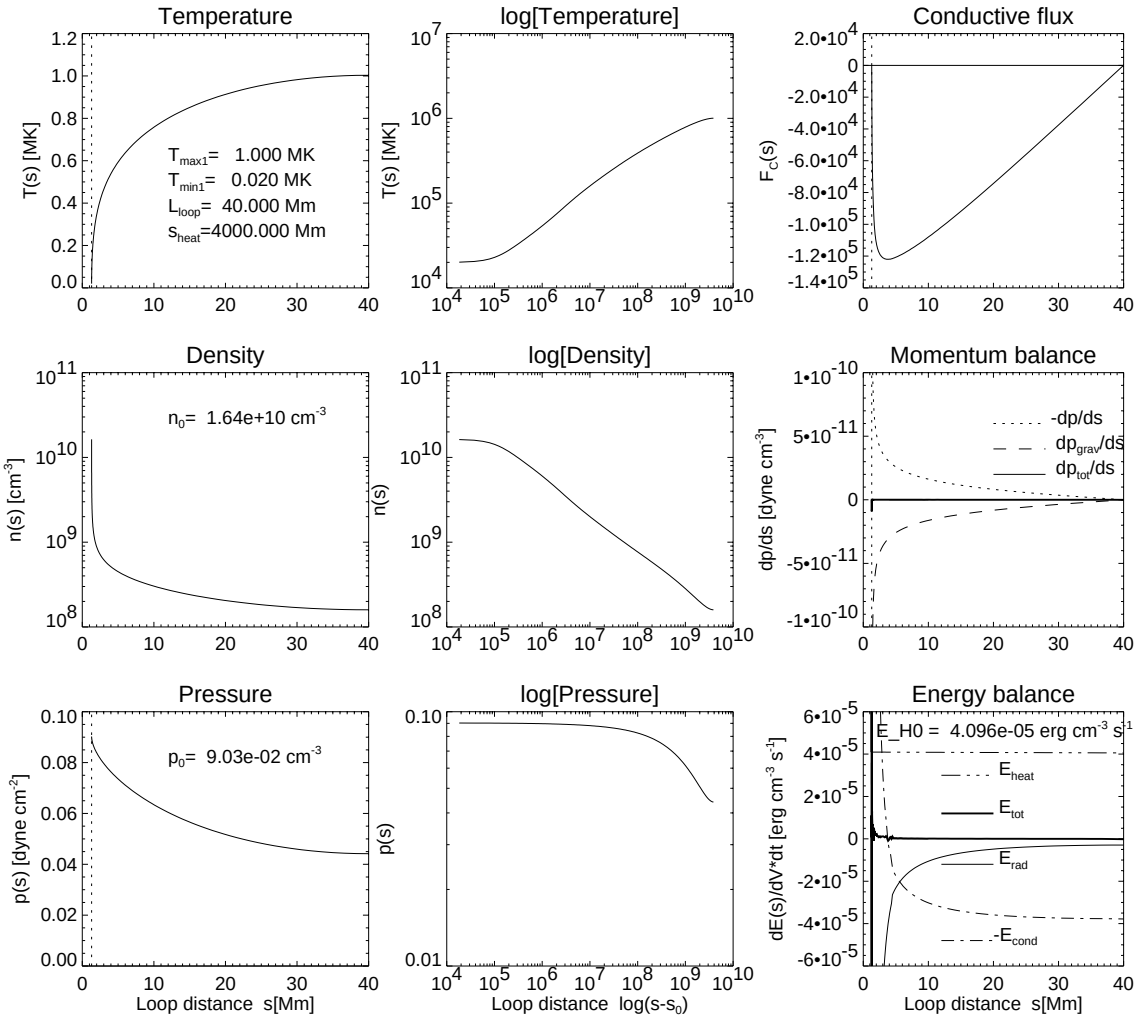


FIG. 1.—Hydrostatic solution of a uniformly heated loop with a loop-top temperature of $T_{\max} = 1.0$ MK and loop half-length of $L = 40$ Mm is shown, computed with the numeric code described in § 3. Note that the transition region is adequately resolved with the numeric code and the boundary conditions of $T(s_0) = 2 \times 10^4$ MK and vanishing flux $dT/ds(s_0) = 0$ are accurately met (*see temperature profile in middle top panel*). The correctness of the numeric solution is warranted by the criteria of zero momentum along the loop (*thick solid line in second right panel*) and zero energy balance along the loop (*thick solid line in bottom right panel*).

with the normalized space coordinate $z = s_0 + (s - s_0)/L$ and $\gamma = 0.5$. Both analytical solutions are shown in Figure 2, agreeing on the $\lesssim 5\%$ level for most parts of the loop, after the pressure in the RTV model has been adjusted by a factor of $p_0 \times 0.2985$. The authors of the MKB model (Martens et al. 2000) note that they have not been able to reproduce the different analytical solution (eq. [17]) given by Rosner et al. (1978), derived under the same assumptions.

No analytical expression or solution has been found for the general case of hydrostatic pressure equilibrium with nonuniform heating. In previous work (Aschwanden, Schrijver, & Alexander 2000b, 2001) we used for an approximation a "generalized" elliptical function, $x^a + y^a = 1$, where the variables $x = (T - T_0)/(T_{\max} - T_0)$ represent a normalized temperature variable and $y = (L - s)/(L - s_0)$ a normalized length variable. We found rough agreement with the exact hydrostatic solution $T(s)$ within an accuracy level of a few percent (Fig. 2 in Aschwanden et al. 2000b). However, this approximation is not sufficient to derive other quantities in scaling laws, because the conductive flux requires the second-order derivative and multiplies uncertainties in the temperature function with a power of $T^{3.5}$ (eq. [10]). We therefore searched for a better approximation and found an extremely well-matching function by employing independent power indices in the "generalized" elliptical function, i.e., $x^a + y^{1/b} = 1$. Explicitly, we parameterize the temperature function with the following approximation:

$$T(s) = T_{\max}\left[1 - \left(\frac{L - s}{L - s_0}\right)^a\right]^b . \qquad (19)$$

We demonstrate the usefulness of this empirically found parameterization in Figure 2, by fitting it to the numerically obtained solution for a particular loop ($T_{\max} = 3$ MK, $L = 100$ Mm) with uniform heating $s_H \gg L$. The difference between the numerical and analytical best fit (obtained for $a = 2.012$ and $b = 0.3215$) amounts to $\lesssim 10^{-3}$ over the entire range of $s_0 < s < L$. The mean and standard deviation are $[T^{\rm ana}(s) - T^{\rm num}(s)]/T_{\max} = 0.0006 \pm 0.0037$. The differences to the analytical solutions of Rosner et al. (1978) and Martens et al. (2000) are within the $\lesssim 5\%$ level, after adjusting the pressure by a factor of $p_0 \times 0.2985$ in the RTV model. Part of the discrepancy between the analytical approximations and numerical solution result from the

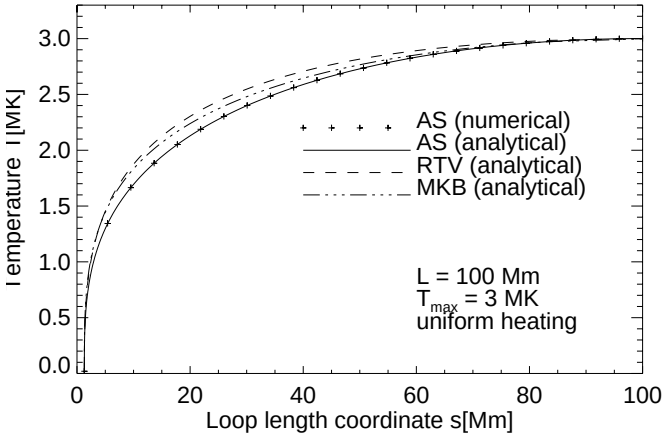


FIG. 2.—Hydrostatic solution of a uniformly heated loop with a loop-top temperature of $T_{\max} = 3$ MK and a half-length of $L = 100$ Mm are shown (*top panel*) from our numerical code (*crosses*), the analytical solution of Rosner, Tucker, & Vaiana (RTV: *dashed line*), the analytical solution of Martens, Kankelborg, & Berger (MKB; *dashed-dotted line*), and the best fit with our analytical function (AS), $T(s) = T_{\max}\{1 - [(L - s)/(L - s_0)]^{2.0074}\}^{0.2858}$ (*solid line*). The base pressure in the RTV model had to be adjusted by a factor of $p_0^{\rm RTV} = p_0 \times 0.2985$ to match our numeric solution.

assumption of constant pressure in the RTV and MKB model, while the remaining discrepancy is attributed to different approximations in the radiative loss function, as discussed below. We are motivated to employ the same formalism for a larger parameter space, since our *Ansatz* of the temperature parameterization (eq. [19]) reproduces the numerical solution with extremely high accuracy ($\lesssim 10^{-3}$) and has a simpler analytical form than the formulations given in equations (17) and (18).

We fitted the analytical expression $T(s)$ (eq. [17]) with the three free variables $a$, $b$, $s_0$ to all of our over 1000 numerical solutions $T^{\rm num}(s)$ in the entire parameter space of $L$, $s_H$, $T_{\max}$ and found that the power indices $a$ and $b$ essentially depend only on a single parameter, the ratio $L/s_H$, but have no dependence on the maximum temperature $T_{\max}$ or the parameters $L$ and $s_H$ separately. In other words, the solution of the temperature function is invariant in $T(s)/T_{\max}$ and $s/L$. The proportionality of $T(s)/T_{\max}$ is also evident in the analytical solutions of Rosner et al. (eq. [17]) and Martens et al. (eq. [18]). We found that the dependence of the temperature power indices $a(L/s_H)$ and $b(L/s_H)$ can best be fitted with the empirical functions:

$$a(L, S_H) = a_0 + a_1 \left(\frac{L}{s_H}\right)^{a_2}, \qquad (20)$$

$$b(L, S_H) = b_0 + b_1 \left(\frac{L}{s_H}\right)^{b_2}. \qquad (21)$$

The best fits are shown in Figure 3, for the subset of hydrostatic solutions with a maximum temperature of $T_{\max} = 3$ MK, sorted by the parameter $L/s_H$. The best-fit coefficients are given in Table 1. The similarity of the coefficients confirms that there is no significant dependence on the loop-top temperature $T_{\max}$, and thus $a$ and $b$ are independent of $T_{\max}$.

We run our analytical approximation of the temperature function (eqs. [19]–[21]) through all 1000 numerical solutions with the same coefficients and find a relative accuracy of $[T(s)/T^{\rm num}(s) - 1] \lesssim 10^{-2}$–$10^{-3}$. Thus, the parameterization of $T(s)$ given with equations (19)–(21) provides us a simple analytical formulation of the temperature function that is sufficiently accurate in the entire parameter space and can be used as a powerful tool to solve the hydrostatic equations.

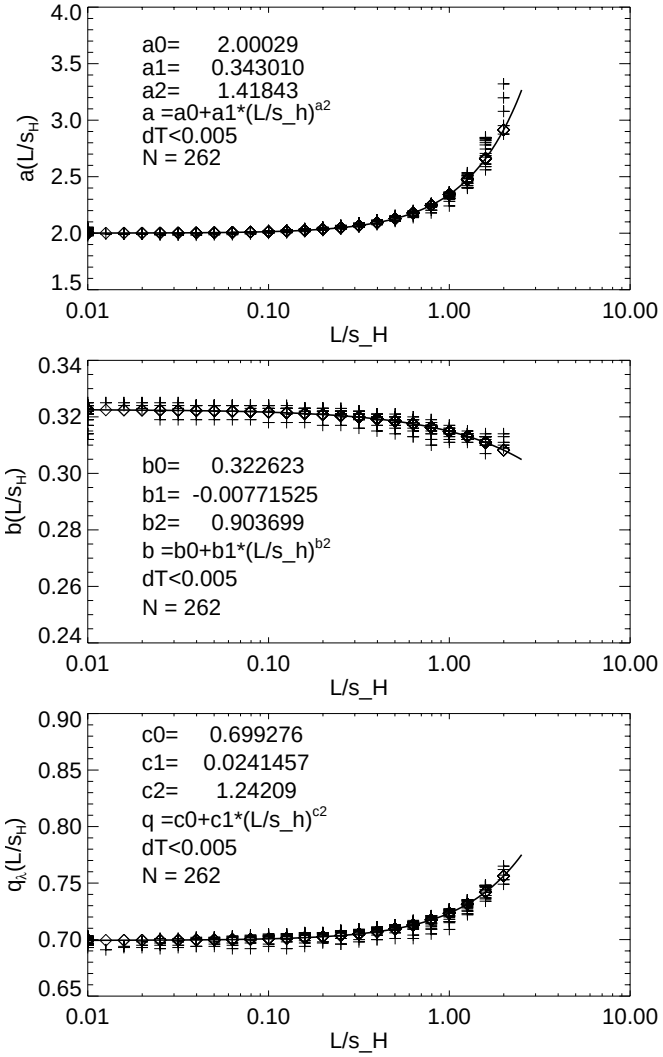


FIG. 3.—Fits of the power indices $a(L/s_H)$ (eq. [20]; *top panel*) and $b(L/s_H)$ (eq. [21]; *middle panel*) in the temperature function $T(s)$ (eq. [19]), and for the scale height factor $q_\lambda(L/s_H)$ (eq. [27]; *bottom panel*) in the pressure function $p(L/s_H)$ (eqs. [25] and [26]), shown for 262 numeric solutions with $T_{\max} = 3$ MK.

### 4.2. *The Pressure Function $p(s)$*

After we have obtained a suitable approximation of the temperature function $T(s)$, we have a much easier way to determine the pressure function $p(s)$, because we can directly integrate the momentum equation (eq. [2]), where the density $n(s)$ can be substituted by the ideal gas law $n(s) = p(s)/2k_{\rm B}T(s)$ (eq. [5]), so that the momentum equation contains only the unknown pressure function $p(s)$,

$$\frac{dp(s)}{dh} = -\frac{p(s)}{\lambda_0}\left[\frac{10^6\ {\rm K}}{T(s)}\right]\left[1 + \frac{h(s)}{R_\odot}\right]^{-2} \qquad (22)$$

TABLE 1
BEST-FIT COEFFICIENTS IN ANALYTICAL APPROXIMATIONS OF HYDROSTATIC SOLUTIONS

| | TEMPERATURE $T_{max}$ | | | | |
|---|---|---|---|---|---|
| COEFFICIENT | 1 MK | 3 MK | 5 MK | 10 MK | EQUATION NUMBER |
| $a_0$ ..... | 2.098 | 2.000 | 2.055 | 2.026 | 38 |
| $a_1$ ..... | 0.258 | 0.343 | 0.328 | 0.298 | |
| $a_2$ ..... | 1.565 | 1.418 | 1.649 | 1.570 | |
| $b_0$ ..... | 0.320 | 0.323 | 0.329 | 0.309 | 39 |
| $b_1$ ..... | −0.009 | −0.008 | −0.009 | −0.009 | |
| $b_2$ ..... | 0.877 | 0.902 | 0.852 | 0.928 | |
| $c_0$ ..... | 0.693 | 0.699 | 0.700 | 0.707 | 45 |
| $c_1$ ..... | 0.026 | 0.024 | 0.014 | 0.029 | |
| $c_2$ ..... | 1.199 | 1.240 | 2.427 | 0.915 | |
| $d_0$ ..... | 1452 | 1416 | 1428 | 1506 | 53 |
| $d_1$ ..... | −0.074 | −0.087 | −0.064 | −0.036 | |
| $d_2$ ..... | −0.030 | −0.044 | 0.000 | 0.001 | |
| $d_3$ ..... | −0.001 | −0.003 | −0.023 | −0.021 | |
| $d_4$ ..... | 0.015 | 0.043 | 0.010 | 0.011 | |
| $e_0$ ..... | $0.686 \times 10^{-6}$ | $0.831 \times 10^{-6}$ | $0.808 \times 10^{-6}$ | $0.707 \times 10^{-6}$ | 54 |
| $e_1$ ..... | 0.558 | 0.848 | 0.847 | 0.685 | |
| $e_2$ ..... | −0.423 | −0.707 | −0.634 | −0.403 | |
| $e_3$ ..... | 0.548 | 0.057 | −0.058 | 0.063 | |
| $e_4$ ..... | 0.156 | 0.365 | 0.361 | 0.145 | |

with the reference scale height for a 1 MK temperature plasma defined by

$$\lambda_0 = \frac{2k_B(10^6\ \mathrm{K})}{\mu m_p g_\odot} = 4.6 \times 10^9\ \mathrm{cm}\ . \tag{23}$$

In the derivation of Serio's scaling law, the pressure function was approximated by an exponential function with a constant pressure scale height $\lambda_p$, which neglects the temperature variation $T(s)$ along the loop and the radial variation of gravity. Because neglect of these effects leads to deviations in the determination of the base pressure $p_0$ and the related scaling law, we retain these dependencies in the form of a height-dependent pressure scale height $\lambda_p(s)$. Integrating the differential equation (eq. [22]) by applying the mean-value theorem to the temperature dependence,

$$\ln\left(\frac{p(s)}{p_0}\right) = -\int_{h_0}^{h} \frac{1}{\lambda_0}\left\{\frac{10^6\ \mathrm{K}}{T(s[h'])}\right\}\left[1+\frac{h'(s)}{R_\odot}\right]^{-2} dh' \approx -\frac{1}{\lambda_0}\frac{1}{q_\lambda}\left\{\frac{10^6\ \mathrm{K}}{T(s[h])}\right\}\int_{h_0}^{h}\left[1+\frac{h'(s)}{R_\odot}\right]^{-2} dh'\ , \tag{24}$$

we can integrate the pressure function

$$p(s) = p_0 \exp\left[-\frac{h(s)-h_0}{\lambda_p(s)}\right]\ , \tag{25}$$

which has the following height-dependent scale height $\lambda_p(s)$:

$$\lambda_p(s) = \lambda_0\left[\frac{T(s)}{10^6\ \mathrm{K}}\right]\left[1+\frac{h(s)}{R_\odot}\right] q_\lambda(L, s_H)\ . \tag{26}$$

The factor $q_\lambda(L, s_H)$ corrects for the mean-value theorem of the temperature dependence $T(s)$, for which we know that it depends primarily on the ratio $(s_H/L)$, according to equations (19)–(21) (see also Fig. 3, *bottom*). Therefore, the only thing left to do for an accurate analytic solution is the numerical determination of the coefficient $q_\lambda$ as a function of $(s_H/L)$. Again, we make an *Ansatz* with three variables $c_0, c_1, c_2$ for this function, similar to equations (19)–(21),

$$q_\lambda(L, s_H) = c_0 + c_1\left(\frac{L}{s_H}\right)^{c_2} \tag{27}$$

and determine these free variables by fitting the analytical pressure function $p(s)$ (eq. [25]) parameterized with height-dependent scale heights $\lambda_p(s)$ (eq. [26]) to the numerical solutions of $p(s)$ to find a best fit of the variables $c_0, c_1, c_2$. The best fit to a subset of numerical solutions with $T_{max} = 3$ MK yields the values $c_0 = 0.699$, $c_1 = 0.024$, $c_2 = 1.240$ (see Fig. 3, *bottom*). In previous work we approximated these correction factor with a constant value, $q_\lambda \approx 0.75$ (eq. [13] in Aschwanden et al. 2000b), which essentially represents $c_0$. We find similar coefficients for the data sets of $T_{max} = 1$, 5, and 10 MK, which are listed in Table 1. Based on these results we have now an accurate analytical approximation of the hydrostatic solutions, specified by the temperature profile $T(s)$ (eqs. [19]–[21]), the pressure profile $p(s)$ (eqs. [25]–[27]), from which follows also the density profile according to the ideal gas law, and

$$n(s) = \frac{p(s)}{k_B T(s)}\ . \tag{28}$$

The only missing scaling parameters are the base pressure $p_0$ and the base heating rate $E_{H0}$, which have to be determined via scaling laws as a function of the independent parameters $(L, s_H, T_{max})$.

### 4.3. *The Scaling Laws*

So far we obtained analytical solutions as a function of five unknown parameters, $L$, $s_H$, $T_{max}$, $E_{H0}$, and $p_0$. While only three parameters are independent (e.g., $L$, $s_H$, $T_{max}$), the dependence of the other two parameters

(e.g., $p_0$ and $E_{H0}$) on the three independent parameters is specified by two scaling laws, i.e., $p_0(L, s_H, T_{\max})$ and $E_{H0}(L, s_H, T_{\max})$. These two scaling laws have been derived in Rosner et al. (1978) and Serio et al. (1981) by integrating the energy equation in two different ways: (1) as spatial integral $\int f(s)ds$ and (2) as temperature integral $\int f(T)dT$ after substituting the conductive flux variable $F_C(T)$.

Rosner et al. (1978) derived the scaling laws under the following assumptions and approximations:

1. Constant pressure, $p(s) = p_0$.
2. Uniform heating, $s_H = \infty$.
3. Radiative loss function is approximated with single power law, $\Lambda(T) \approx \Lambda_0 T^{-1/2}$, with $\Lambda_0 = 10^{-18.81}$ erg cm$^3$ s$^{-1}$.
4. Auxiliary function $f_H(T) \ll f_R(T)$, i.e., $\int T^{5/2} E_H(T)dT \ll \int T^{5/2} E_R(T)dT$.
5. Neglect height dependence of solar gravitation $g(h) = g_\odot(1 + h/R_\odot)^{-2}$ (eq. [9]).
6. Footpoint in photosphere ($s_0 = 0$).

The scaling laws can generally be expressed as a function of the independent variables $[L_0, s_H, T_{\max}]$ by

$$p_0(L_0, s_H, T_{\max}) = \frac{1}{L_0}\left(\frac{T_{\max}}{S_1}\right)^3 , \quad (29)$$

$$E_{H0}(L_0, s_H, T_{\max}) = L_0^{-2} T_{\max}^{7/2} S_2 . \quad (30)$$

where we denoted the footpoint-apex distance by $L_0 = L - s_0$. Under the assumptions and approximations listed above, Rosner et al. (1978) derived the following constants for the expressions $S_1$ and $S_2$:

$$S_1^{\rm RTV} = 1400 , \quad (31)$$

$$S_2^{\rm RTV} = 0.95 \times 10^{-6} . \quad (32)$$

We show the comparison of the RTV scaling laws with our numerical solutions as a function of $L/s_H$ in Figure 4 (*top panels*). The scaling law for the base pressure agrees with the numerical solutions within $(p_0^{\rm RTV}/p_0) \approx 0.9 \pm 0.1$ for near-uniform heating ($L/s_H \lesssim 1$). The scaling law for the base heating rate agrees with the numerical solutions within $(E_{H0}^{\rm RTV}/E_{H0}) \approx 0.8 \pm 0.3$ for near-uniform heating ($L/s_H \lesssim 1$) but yields too low heating rates down to fractions of 0.2 for short heating scale lengths (at $L/s_H \lesssim 2$).

Serio et al. (1981) generalized the RTV scaling laws for variable pressure (owing to gravity) and nonuniform heating but retained the other approximations from the derivation of Rosner et al. (1978). Thus, Serio's derivation is subject to the same set of assumptions and approximations except the first two:

1. The pressure is assumed to be an exponential function of the loop length, $p(s) \approx p_0 \exp(-s/s_p)$, with $s_p = \lambda_0 T_{\rm MK}$. This approximation neglects the temperature variation $T(s)$ along the loop, and thus the variation of the pressure scale height $\lambda_p(s)$ (see eq. [26]).
2. The height dependence in the pressure function is approximated by the semicircular loop coordinate $s$, $p(h) \approx p(s)$.

Note that the numerical calculations of coefficients $\alpha$, $\beta$, $\alpha'$, $\beta'$ (eqs. [3.7]–[3.8] in Serio et al. 1981) are optimized based on numerical solutions in some (unspecified) parameter space, which probably covers a different parameter regime than our numerical solutions. Moreover, Serio et al. calculate hydrostatic solutions for loops with an expansion factor of 5, while we calculate cases for constant as well as expanding cross sections separately.

Serio's scaling laws have the same basic dependence on $L_0$ and $T_{\max}$ as the RTV laws (eqs. [29]–[30]) but differ in the scaling law expressions $S_1$ and $S_2$ (eqs. [31]–[32]),

$$S_1^{\rm Serio} = 1400 \exp\left(-0.08\frac{L_0}{s_H} - 0.04\frac{L_0}{s_p}\right) , \quad (33)$$

$$S_2^{\rm Serio} = 0.95 \times 10^{-6} \exp\left(0.78\frac{L_0}{s_H} - 0.36\frac{L_0}{s_p}\right) , \quad (34)$$

where we denoted $s_p = \lambda_0 T_{\rm MK}$ and $T_{\rm MK} = T_{\max}/10^6$ MK. While Serio's generalization accounts for nonuniform heating and pressure variation, the approximations made in the derivation lead to differences from the proper numerical solutions, as shown in Figure 4 (*middle row*) relative to our exact numerical solutions. The agreement with our numerical solutions of $p_0$ and $E_{H0}$ are within $1.0 \lesssim p_0^{\rm Serio}/p_0 \lesssim 1.4$ and $0.9 \lesssim E_{H0}^{\rm Serio}/E_{H0} \lesssim 1.3$, with some extreme deviations down to $E_{H0}^{\rm Serio}/E_{H0} \gtrsim 0.2$.

In order to achieve a higher level of accuracy between the numerical hydrostatic solutions and the scaling law approximations, we add two additional correction terms to Serio's expressions (eqs. [33] and [34]), leading to five coefficients for each of the two scaling laws, called $d_i$ and $e_i$, $i = 0, \ldots, 4$, respectively:

$$S_1^{AS} = d_0\left[\exp\left(d_1\frac{L_0}{s_H} + d_2\frac{L_0}{s_p}\right) + d_3\frac{L_0}{s_H} + d_4\frac{L_0}{s_p}\right] , \quad (35)$$

$$S_2^{AS} = e_0\left[\exp\left(e_1\frac{L_0}{s_H} + e_2\frac{L_0}{s_p}\right) + e_3\frac{L_0}{s_H} + e_4\frac{L_0}{s_p}\right] . \quad (36)$$

We determine these 10 coefficients $d_i$ and $e_i$ by minimizing the differences of the scaling law expressions $p_0(d_i)$ (eqs. [29] and [35]) [and $E_{H0}(e_i)$ (eqs. [30] and [36])] to the numerical solutions $p_0^{\rm num}$ [and $E_{H0}^{\rm num}$] from our 1000 numerical runs, which cover the parameter space of [$T_{\max} = 1$–10 MK, $L = 4$–400 Mm, $s_H = 4$–400 Mm]. The best-fit values of the coefficients $d_i$ and $e_i$, $i = 0, \ldots, 4$ are tabulated in Table 1, for different temperatures $T_{\max} = 1$, 3, 5, and 10 MK. If one uses just one set of coefficients (say from $T_{\max} = 3.0$ MK in Table 1) for a larger temperature range, the accuracy of the scaling laws is about $\lesssim 5\%$ in the temperature of $T = 2$–5 MK and degrades to $\approx 10\%$–$20\%$ in the temperature range of $T = 1$–10 MK. For a higher accuracy in the order of a few percent, a spline interpolation of the coefficients (given in Table 1) as a function of $T_{\max}$ is recommended. These empirical scaling laws (eqs. [35] and [36]) provide a best fit to the numerical solutions within an accuracy of a few percent (see Fig. 4, *bottom panels*). The functional dependence of these scaling laws is shown in Figure 5 for $E_{H0}(L, s_H, T_{\max})$, and in Figure 6 for $p_0(L, s_H, T_{\max})$, respectively.

### 4.4. *Choice of Independent Parameters* $[L, s_H, E_{H0}]$

The analytical formulation of the scaling law derived by Serio et al. (1981) requires the independent parameter set $[L, s_H, T_{\max}]$, because the pressure scale height $s_p = \lambda_0(T_{\max}/10^6$ K) depends on $T_{\max}$, so that the second scaling law (eqs. [30] and [34]) can only be expressed explicitly for $E_{H0}(L, s_H, T_{\max})$, but not explicitly in the form of $T_{\max}(L, s_H, E_{H0})$. The same is also true for our modified

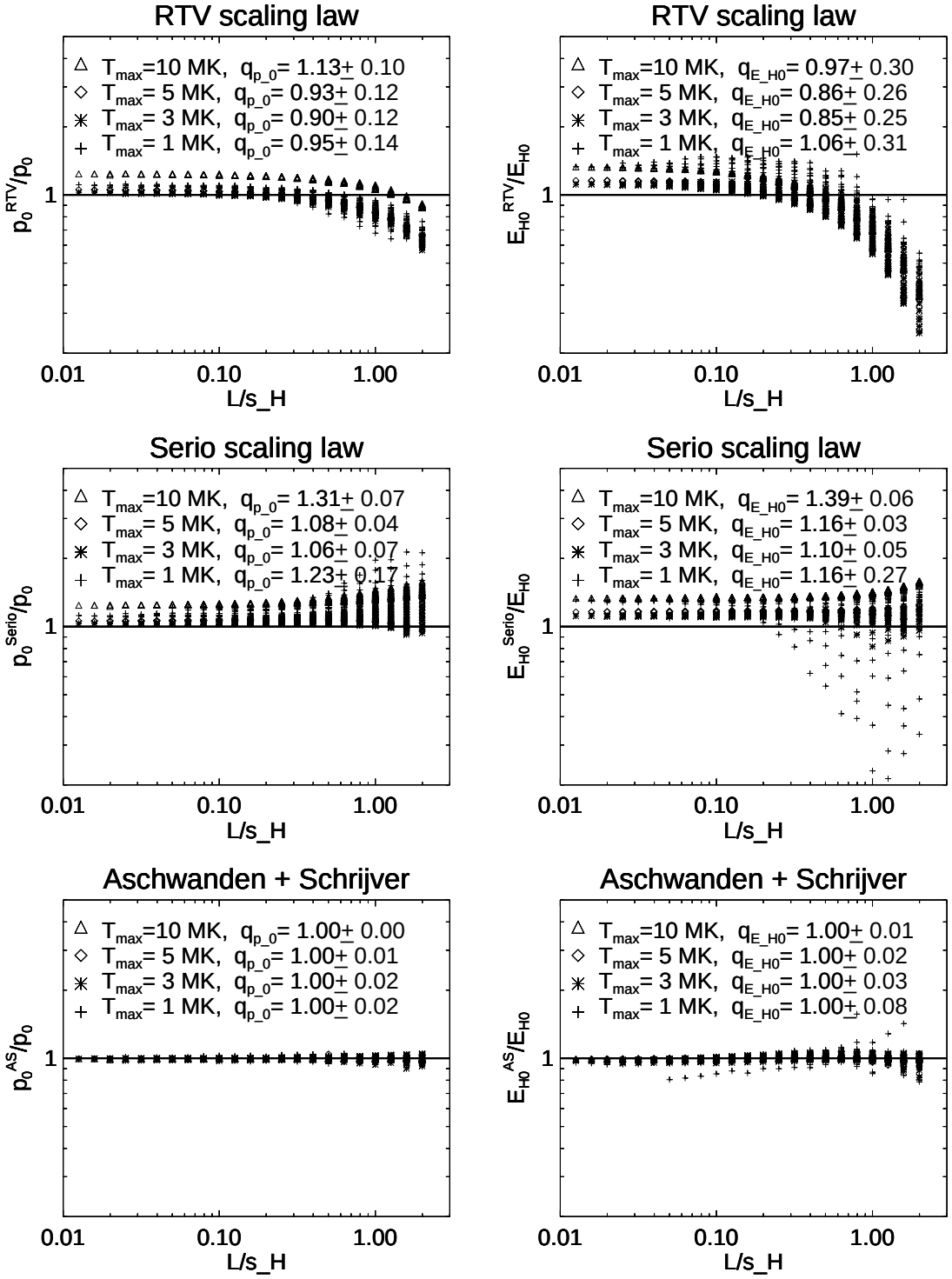


FIG. 4.—Accuracy of the two scaling laws $p_0(L, s_H, T_{\max})$ (*left column*) and $E_{H0}(L, s_H, T_{\max})$ (*right column*) is shown as a function of the parameter $(L/s_H)$, for the Rosner-Tucker-Vaiana scaling law for uniform heating (*top*), for Serio's scaling law for nonuniform heating (*middle*), and for the analytical approximations in this study (*bottom*). All ratios are normalized by the values of the proper numerical solutions for $p_0$ and $E_{H0}$. In each panel we show the four subsets for different temperatures ($T_{\max} = 1, 3, 5, 10$ MK) with separate symbols, and the averages and standard deviations of the ratios are given for each temperature separately.

scaling law (eqs. [30] and [36]). However, from a physical point of view, the choice of the independent parameter set $[L, s_H, E_{H0}]$ is more natural, because the heating function specified by $[s_H, E_{H0}]$ defines the energy input, while the temperature $T_{\max}$ represents the final outcome of a relaxation process when evolving into a hydrostatic equilibrium. This is especially important for hydrodynamic processes, where the input can be defined as initial boundary condition, while the parameters of the final outcome generally cannot be predicted. Only for hydrostatic solutions, the choice of independent parameters are exchangeable in the scaling law relations.

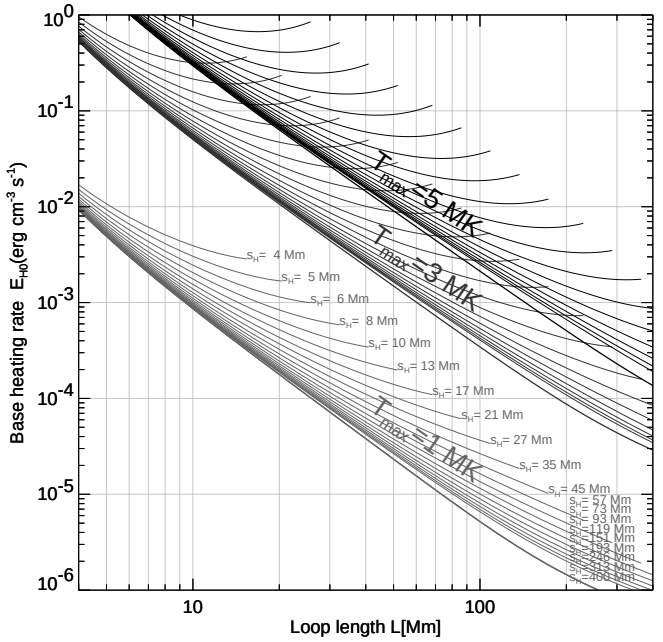


FIG. 5.—Scaling law for the base heating rate $E_{H0}(L, s_H, T_{\max})$ according to our analytical approximation (eqs. [30] and [36]).

How do we go to an analytical approximation of hydrostatic solutions and scaling laws based on the independent parameter set $[L, s_H, E_{H0}]$? Essentially, we have to invert the energy scaling law to obtain an explicit expression for $T_{\max}(L, s_H, E_{H0})$. Unfortunately, $T_{\max}$ occurs as power $T_{\max}^{7/2}$ in equation (30) and at the same time in the exponent $\exp(\ldots s_p[T_{\max}])$ in equations (34), which represents a transcendental equation for $T_{\max}$ that is not analytically invertible. However, $T_{\max}$ can be inverted numerically. For convenience we derived also a single expression for the scaling law inversion, which gives the loop-top maximum temperature $T_{\max}$ explicitly as a function of the three independent parameters $(L_0, s_H, E_{H0})$, where $L_0 = L - s_0$,

$$T_{\max}(L_0, s_H, E_{H0}) = 55.2\left[E_{H0}^{0.977} L_0^2 \exp\left(-0.687\frac{L_0}{s_H}\right)\right]^{2/7}, \quad (37)$$

which approximates our 1000 numerical solutions of the scaling law (in the temperature range of $T = 1$–10 MK) with an average accuracy of $\approx 3\%$.

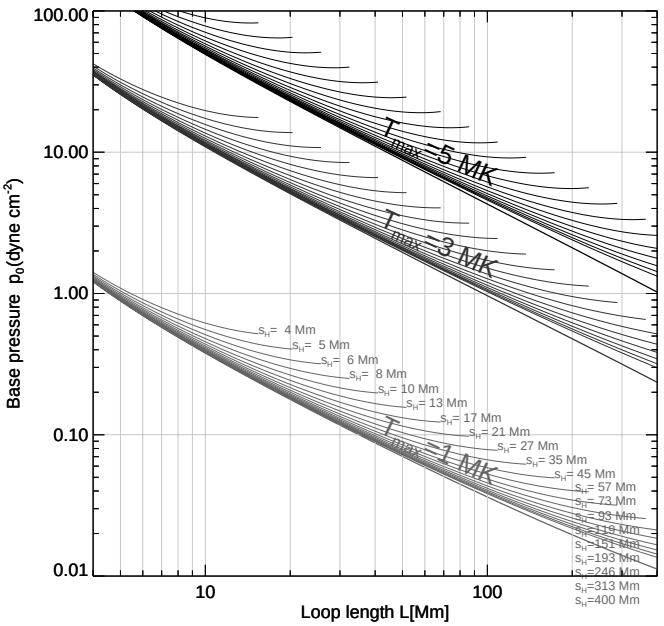


FIG. 6.—Scaling law for the base pressure $p_0(L, s_H, T_{\max})$ according to our analytical approximation (eqs. [29] and [35]).

### 4.5. *The Radiative Loss Function and Elemental Abundances*

One of the major uncertainties in hydrostatic models are the assumptions on elemental abundances, because they can significantly change the radiative loss function $\Lambda(T)$ (eq. [12]). In our standard calculations we adopted the loss function $\Lambda(T)$ calculated by Tucker & Koren (1971), which was approximated by Rosner et al. (1978) by piecewise power laws. This radiative loss function is based on the work of J. Raymond (e.g., reproduced in Golub & Pasachoff 1997), which is consistent (within a factor of $\lesssim 3$) with other published radiative loss functions (e.g., Cook et al. 1989) based on chromospheric abundances (e.g., Meyer 1985). A comparison of different calculations of currently published radiative loss functions is shown in Figure 7. Recent developments include the *First-ionization potential (FIP)* effect, which leads to substantial correction (up to a factor of 10) of the radiative loss function $\Lambda(T)$ at temperatures of $T = 1.0$ MK (Martens et al. 2000) due to the enhanced coronal iron abundance (Feldman 1992). This effect can produce up to a factor of 3 lower electron densities in hydrostatic solutions in cases where radiative loss dominates over conductive loss.

In order to demonstrate the effects of assumptions on elemental abundances on hydrostatic solutions we calculate a hydrostatic solution of a coronal loop for two different elemental abundances: (1) for the radiative loss function based on chromospheric abundances (Rosner et al. 1978), and (2) for coronal abundances with enhanced iron (Martens et al. 2000). The hydrostatic solution with chromospheric abun-

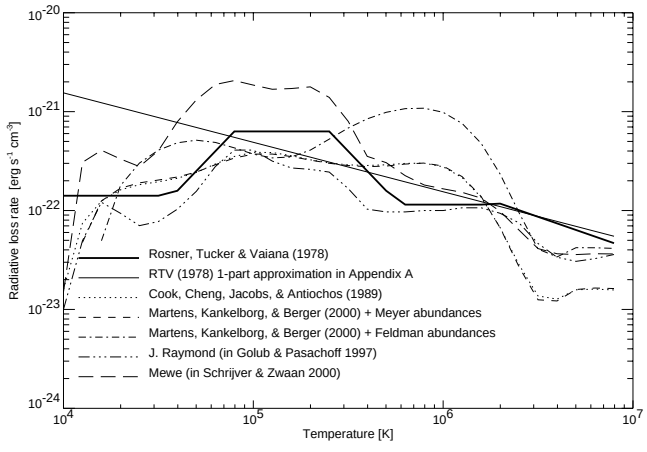


FIG. 7.—Compilation of radiative loss functions. The one-piece power-law approximation (*thin solid line*) was used in the derivation of the RTV and Serio's scaling laws (eqs. [29]–[34]).

dances yields a somewhat higher temperature function and a massively enhanced density and pressure function (Fig. 8, *black curves*), while the solution based on coronal abundances yields a lower density and pressure (Fig. 8, *gray curves*), due to the enhanced radiative losses of the iron element at temperatures around $T \approx 1$ MK. Thus, this uncertainty by about a factor of 2 in the assumptions on elemental abundances far outweighs the inaccuracy of our analytical approximation to the numerical hydrostatic solutions within the few percent level.

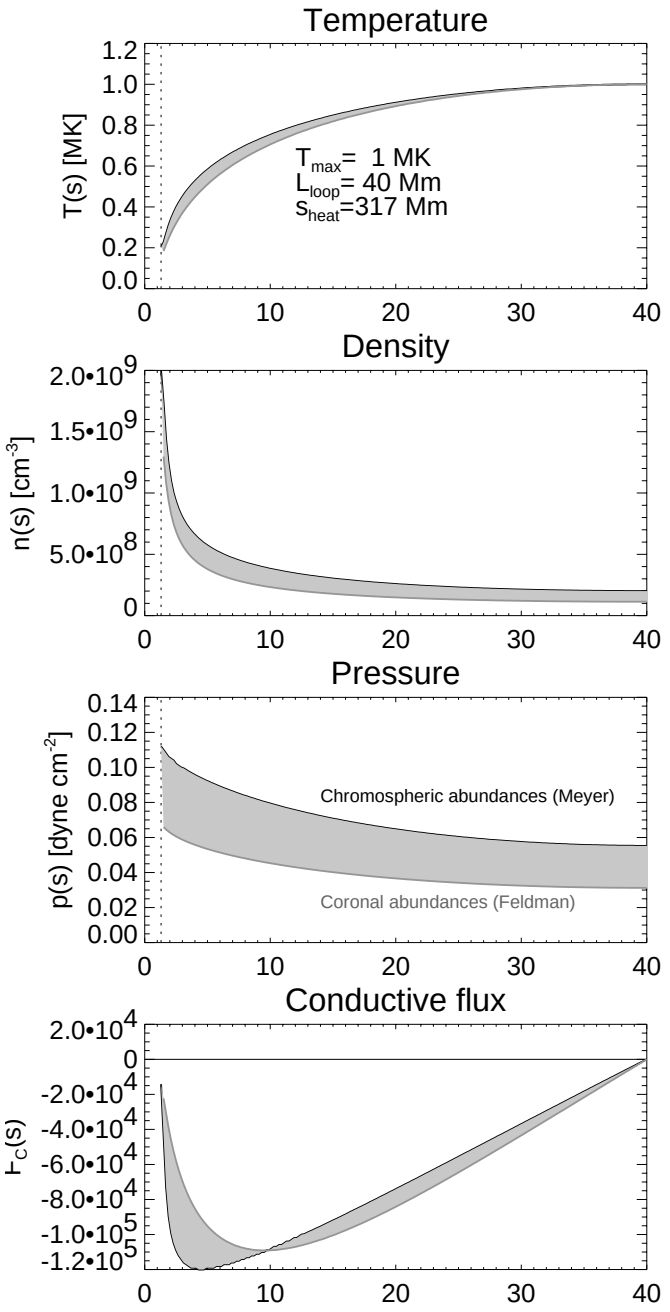


FIG. 8.—Comparison of hydrostatic solutions computed for two different radiative loss functions: for the RTV six–power-law approximation (Fig. 7, *thick line*) and chromospheric abundances according to Meyer (1985), and for the same radiative loss function and coronal abundances according to Feldman (1992). The difference in the solution is shown in gray.

## 5. GENERALIZED HYDROSTATIC SOLUTIONS

In this section we generalize our analytical approximations of the hydrostatic solutions to allow applications in a wider range of observational circumstances. We generalize the solutions for extremely small heating scale lengths, for inclined loops, for loops with variable cross sections, and for slow velocity flows. These generalizations have been tested in part of the previously used parameter space, which covers a temperature range of $T = 1$–$10$ MK.

### 5.1. *Small Heating Scale Heights*

In the previous sections we covered a large parameter space with spatial scales in the range of 4–400 Mm for $L$ and $s_H$, but we excluded extremely small heating scale lengths, say with $s_H \lesssim L/3$. Already Serio et al. (1981) subdivided hydrostatic solutions into two classes with the same criterion: class I are loops with the temperature maximum at the loop top (which is the case for $s_H \gtrsim L/3$), and class II are loops with the temperature maximum at some intermediate position between the loop top and footpoints (which is the case for $s_H \lesssim L/3$). We show numerical solutions of hydrostatic temperature profiles from $s_H = L$ down to $s_H = L/25$ in Figure 9 (*solid lines*). The temperature maximum clearly moves downward the loop with decreasing heating scale length ratio $s_H/L$, and a larger segment of the loop becomes near isothermal. Because our previous temperature approximation with a generalized ellipse function $x^a + x^{1/b} = 1$ has its maximum by definition at the loop top, the same approximation cannot represent loops with an intermediate temperature maximum. However, a correction can be added that makes the analytical approximation valid down to extremely short heating scale lengths of $s_H \gtrsim L/25$. Because the temperature solution was found to be nearly invariant with respect to the normalized temperature $T(s)/T_{\max}$ and spatial coordinate $z = (s - s_0)/(L - s_0)$, the correction term scales only with the ratio $s_H/L$. We found a good approximation within the $\lesssim 1\%$ level (Fig. 9, *dashed lines*) with the

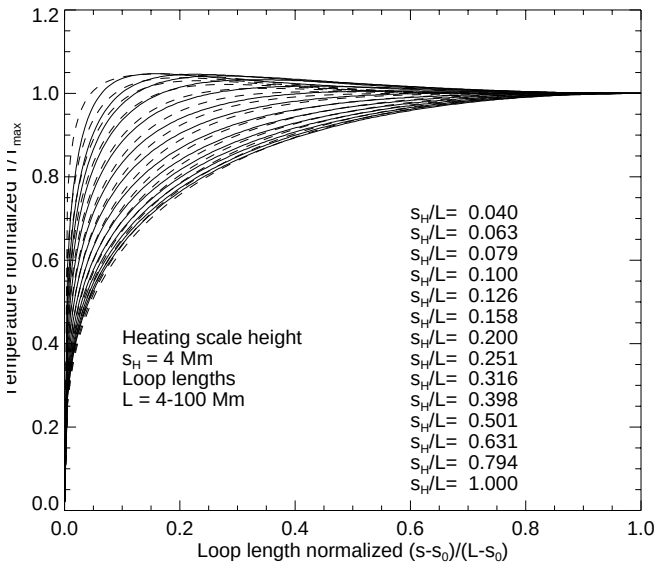


FIG. 9.—Hydrostatic solutions for extremely short heating scale lengths, $s_H/L = 0.04, \ldots, 1.0$. The numeric solutions are shown in solid lines, and the analytical approximation (eqs. [40] and [41]) in dashed lines.

following corrected temperature function:

$$z = \left( \frac{L - s}{L - s_0} \right) , \tag{38}$$

$$T'(s) = T_{\max}[1 - z^a]^b \left[ 1 + 0.5^{10} \log\left( \frac{L}{s_H} \right) (1 - z) z^5 \right] . \tag{39}$$

Because our analytical approximations of the hydrostatic solutions and scaling laws are all expressed in terms of the temperature solution (Table 2), the standard temperature approximation $T(s)$ can simply be replaced by the corrected function $T'(s)$ in this formalism, and the analytical approximations for the pressure function $p(s)$ and density $n(s)$ as well as the resulting scaling laws will automatically be corrected as a function of the improved temperature function $T'(s)$. This correction, however, needs only to be applied for extremely short heating scale lengths, in the range of $s_H < L/3$.

### 5.2. *Inclined Loops*

Most of the observed coronal loops have some inclination of the average loop plane with respect to the vertical on the solar surface. For instance, a bundle of 30 stereoscopically reconstructed active region loops were found to have an almost uniform distribution of inclination angles in the range of $\theta = -49^\circ \ldots +69^\circ$ (Aschwanden et al. 1999). While the gravitational scale height is strictly measured in vertical direction, the effective scale height in the loop plane varies with the cosine of the vertical scale height, so we can define an effective gravity component along the loop,

$$g_{\rm eff} = g_\odot \cos\theta . \tag{40}$$

TABLE 2

Summary of Analytical Formulae to Calculate Hydrostatic Solutions and Scaling Laws

| Description | Formula |
|---|---|
| **Constants:** | |
| Height of loop base | $s_0 = 1.3 \times 10^8$ cm |
| Temperature at loop base | $T_0 = 2.0 \times 10^4$ K |
| Solar radius | $R_\odot = 6.96 \times 10^{10}$ cm |
| Solar gravity | $g_\odot = 2.74 \times 10^4$ cm s$^{-2}$ |
| Spitzer conductivity | $\kappa = 9.2 \times 10^{-7}$ erg s$^{-1}$ cm$^{-1}$ K$^{-7/2}$ |
| **Independent variables:** | |
| Loop half-length | $L$ (cm) |
| Heating scale length | $s_H$ (cm) |
| Loop-top temperature | $T_{\max}$ (K) |
| Base heating rate | $E_{H0}$ (ergs cm$^{-3}$ s$^{-1}$) |
| Loop plane inclination angle | $\theta$ (deg) |
| Loop expansion factor | $\Gamma \geq 1$ |
| Choice 1: $[L, s_H, T_{\max}, \theta, \Gamma]$ | |
| Choice 2: $[L, s_H, E_{H0}, \theta, \Gamma]$ | $\mapsto T_{\max} \approx 55.2 \{ E_{H0}^{0.977} L_0^2 \exp[-0.687(L_0/s_H^\Gamma)] \}^{2/7}$ |
| **Dependent parameters:** | |
| Half-loop length above base | $L_0 = L - s_0$ |
| Loop height | $h_1 = (2L/\pi)$ |
| Subphotospheric zero point | $s_{\rm sub} = L[(\pi/2)/\arcsin(1/\Gamma^{1/2}) - 1]^{-1}$ |
| Equivalent heating scale length | $s_H^\Gamma = s_H[1 + (\Gamma - 1)(s_H/L)]^{-1/2}$ if $(s_H \leq L, \Gamma \geq 1)$ |
| | $s_H^\Gamma = s_H[(\Gamma - 1)]^{-1/2}$ if $(s_H > L, \Gamma > 1)$ |
| Temperature index 1 | $a = a_0 + a_1 (L_0/s_H^\Gamma)^{a_2}$ |
| Temperature index 2 | $b = b_0 + b_1 (L_0/s_H^\Gamma)^{b_2}$ |
| Scale height factor | $q_\lambda = c_0 + c_1 (L_0/s_H^\Gamma)^{c_2}$ |
| Effective gravity | $g_{\rm eff} = g_\odot \cos\theta$ |
| Effective scale height | $\lambda_0 = (2k_{\rm B}10^6[{\rm K}]/\mu m_p g_{\rm eff}) = 4.6 \times 10^9 (1/\cos\theta)$ cm |
| Serio scale height | $s_p = \lambda_0 (T_{\max}/10^6\ {\rm K})$ |
| Scaling law factor 1 | $S_1 = d_0 \{ \exp[d_1(L_0/s_H^\Gamma) + d_2(L_0/s_p)] + d_3(L_0/s_H^\Gamma) + d_4(L_0/s_p) \}$ |
| Scaling law factor 2 | $S_2 = e_0 \{ \exp[e_1(L_0/s_H^\Gamma) + e_2(L_0/s_p)] + e_3(L_0/s_H^\Gamma) + e_4(L_0/s_p) \}$ |
| Base heating rate (for Choice 1) | $E_{H0} = L_0^{-2} T_{\max}^{7/2} S_2$ |
| Base pressure | $p_0 = L_0^{-1} (T_{\max}/S_1)^3$ |
| **Analytical approximations:** | |
| Normalized length coordinate | $z(s) = (L - s)/(L - s_0)$ |
| Height (in loop plane) | $h'(s) = h_1 \sin(s/h_1)$ |
| Loop cross section area | $A(s) = \Gamma \sin^2 [(\pi/2)(s + s_{\rm sub})/(L + s_{\rm sub})]$ |
| Temperature (if $s_H^\Gamma/L > 0.3$) | $T(s) = T_{\max}[1 - z^a]^b$ |
| Temperature (if $s_H^\Gamma/L \leq 0.3$) | $T(s) = T_{\max}[1 - z^a]^b [1 + 0.5^{10} \log(L/s_H)(1 - z) z^5]$ |
| Conductive flux | $F_C(s) = -\kappa T(s)^{5/2} [dT(s)/ds]$ |
| Pressure scale height | $\lambda_p(s) = \lambda_0 [T(s)/10^6\ {\rm K}][1 + h'(s)/R_\odot] q_\lambda$ |
| Pressure | $p(s) = p_0 \exp\{-[h'(s) - h'(s_0)]/\lambda_p(s)\}$ |
| Density | $n(s) = [p(s)/2k_{\rm B}T(s)]$ |

The conceptually simplest method to include the inclination of the loop plane in hydrostatic solutions is to use the effective gravity component for calculations of hydrostatic solutions in the inclined loop plane. All we have to do is to replace the gravity $g_\odot$ by the effective gravity $g_{\rm eff}$ in the equation for the reference scale height $\lambda_0$ in equation (26) and to rename the height variable $h(s)$ in equation (13) by $h'(s)$ to indicate that $h'$ is measured in the loop plane, which is then related to the vertical height $h$ by $h = h' \cos\theta$. The correction of the effective scale height $\lambda_0$ is then carried to the pressure scale height $\lambda_p(s)$ (eq. [26]) and the resulting pressure $p(s)$ (eq. [25]) and density function $n_e(s)$ (eq. [28]). This generalization for inclined loop planes is implemented in the summary of analytical formulae in Table 2.

### 5.3. *Loops with Expanding Cross Sections*

Vesecky et al. (1979) computed hydrostatic solutions for loops with expansion factors and found that the temperature profile does not change much, but the densities increase somewhat for higher expansion factors $\Gamma$. So far we discussed only hydrostatic solutions of loops with constant cross sections. However, we developed a numeric code (§ 3) that can compute hydrostatic solutions for loops with arbitrary cross sections, e.g., characterized by an expansion factor $\Gamma$ (eqs. [15] and [16]). We compute now a few cases with such expansion factors of $\Gamma = 1$, 2, 5, 10. The resulting hydrostatic solutions for the temperature $T_e(s)$ and density $n_e(s)$ are shown in Figure 10. From the temperature solutions we see that higher loop expansion factors $\Gamma$ (Fig. 10) have about the same effect on temperature profiles as shorter heating scale lengths $s_H$ (Fig. 9). We can therefore define an equivalent heating scale length $s_H^\Gamma$ by comparing the heating power $P(s)$ integrated over the loop cross section $A(s)$ in a loop with a constant cross section, $P(s) = E_H(s)A_0$, with that of an expanding loop, $P(s) = E_H^\Gamma(s)A^\Gamma(s)$,

$$E_{H0} \exp\left(-\frac{h}{s_H}\right) A_0 = E_{H0}^\Gamma \exp\left(-\frac{h}{s_H^\Gamma}\right) A(s) \; . \qquad (41)$$

At the footpoints we can use a (linear) first-order Taylor expansion of the heating function $E_H(s)$ (eq. [11]) and the area cross section function $A(s)$ (eq. [15]),

$$E_H(s) \approx E_{H0}\left(1 - \frac{h}{s_H} + \ldots\right) , \qquad (42)$$

$$E_H^\Gamma(s) \approx E_{H0}^\Gamma\left(1 - \frac{h}{s_H^\Gamma} + \ldots\right) , \qquad (43)$$

$$A(s) \approx A_0\left[1 + (\Gamma - 1)\frac{h}{L} + \ldots\right] . \qquad (44)$$

Inserting these first-order expansions into the equivalence equation (eq. [49]) we find the following relation:

$$s_H^{\Gamma,\rm foot} = \begin{cases} s_H \Big/ \left[1 + (\Gamma - 1)\dfrac{s_H}{L}\right] , & \text{for } s_H \le L \; , \\ L/[(\Gamma - 1)] \; , & \text{for } s_H \gg L \; . \end{cases} \qquad (45)$$

This reduced heating scale length compensates for the diverging cross section at the loop footpoints, while the cross section is nearly constant at the loop top (given the $\sin^2$-function in eq. [15] for the cross section variation). Thus, the temperature profile at the loop top is similar to that of constant cross sections, and no compensation is needed in the heating scale length,

$$s_H^{\Gamma,\rm top} \approx s_H \; . \qquad (46)$$

Comparing the numerical hydrostatic solutions of loops with variable cross sections with those of constant cross sections, we found that the overall behavior of the equivalence heating scale length $s_H^\Gamma$ is reproduced rather well by the geometric mean from the loop-top and footpoints, i.e.,

$$s_H^\Gamma \approx \sqrt{s_H^{\Gamma,\rm foot} s_H^{\Gamma,\rm top}} \; . \qquad (47)$$

Thus, a useful approximation of the equivalent heating scale height $s_H^\Gamma$ to compensate for the loop expansion factor $\Gamma$ is

$$s_H^\Gamma = \begin{cases} \dfrac{s_H}{\sqrt{1 + (\Gamma - 1)(s_H/L)}} \; , & \text{for } s_H \le L, \, \Gamma \ge 1 \; , \\ \dfrac{L}{\sqrt{(\Gamma - 1)}} \; , & \text{for } s_H > L, \, \Gamma > 1 \; . \end{cases} \qquad (48)$$

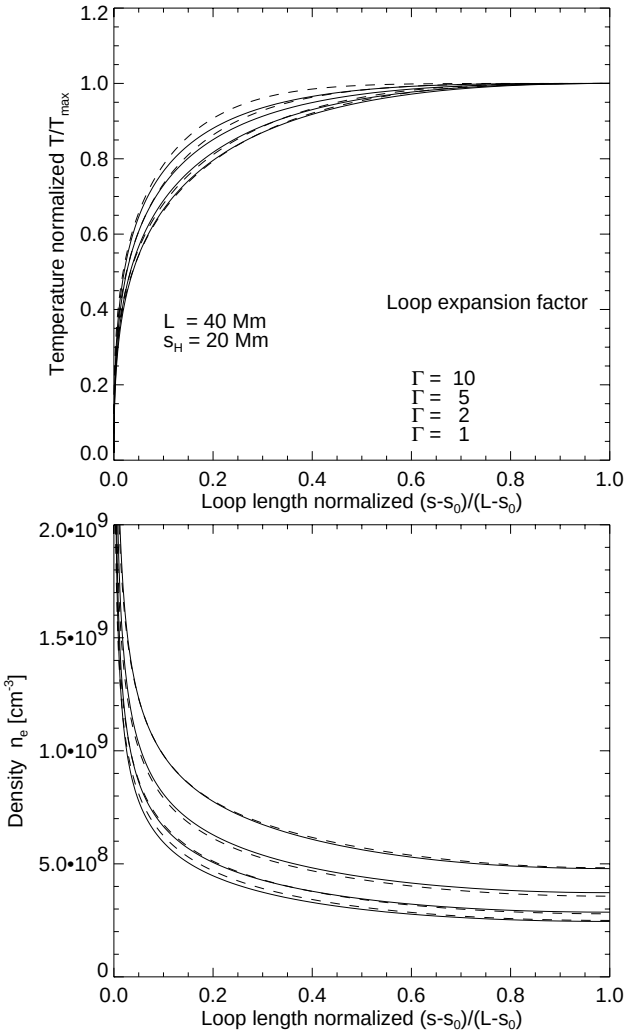


FIG. 10.—Hydrostatic solutions of the temperature $T(s)$ (*top*) and density $n_e(s)$ (*bottom*) for loops with geometric expansion factors $\Gamma = 1$, 2, 5, 10. The exact numeric solutions are plotted with solid lines, the analytical approximations with dashed lines. Note that the analytical approximations are accurate to within a few percent for $\Gamma = 1$–10.

With this concept we have a simple correction formula for the hydrostatic solutions of loops with expanding loop cross sections. Essentially, we can use the same hydrostatic solutions of loops with constant cross sections, say for a parameter set of $[E_{H0},\ s_H^{\Gamma},\ L,\ \Gamma = 1]$, to obtain a good approximation for a loop with expansion factor $\Gamma$. We demonstrate this in Figure 10, where the corresponding approximations (*dashed lines*) are shown along with the exact numerical solutions (*solid lines*). The approximations match the exact numerical solutions with an accuracy of a few percent for $\Gamma = 1$–10 in coronal heights. So, the expansion factor $\Gamma$ of loops has an effect similar to that of a shorter heating scale length, i.e., the temperature profile is more isothermal in the upper part of the loops and the base pressure increases, compared with a loop with constant cross section. For very high expansion factors $\Gamma$, the temperature maximum moves from the loop top downward, similar to the case of shorter heating scale lengths, $s_H \ll L$.

### 5.4. *Differential Emission Measure Modeling*

For modeling of stellar atmospheres one can use magnetic field models and populate individual magnetic field lines with hydrostatic flux tubes. The total differential emission measure (DEM) distribution from a stellar atmosphere can then be computed by adding up all (spatially unresolved) flux tubes, yielding a global DEM distribution $dEM(T)/dT$ (e.g., Schrijver & Aschwanden 2002; Peres et al. 2000, 2001). The DEM distribution of a single loop is defined by

$$\frac{dEM(T)}{dT} = A(T) n_e^2(s[T]) \frac{ds[T]}{dT} \ , \tag{49}$$

which can be calculated by inverting the temperature profile $T(s)$ and using the density function $n_e(s)$ from our hydrostatic solutions. One question is how accurate our analytical solutions match the numerical solutions of such DEM distributions. We calculated these DEM distributions for both our numerical solutions $dEM(T)/dT_{\rm num}$ as well as for our analytical approximations $dEM(T)/dT_{\rm ana}$ and tested the accuracy of the mean ratio. Figure 11 shows a representative set of DEMs, calculated for four different temperatures ($T_{\rm max} = 1$, 3, 5, 10 MK) and four different loop expansion factors ($\Gamma = 1$, 3, 5, 10), for a loop with a length of $L = 40$ Mm and a heating scale height of $s_H = 20$ Mm (Fig. 11, *left panel*) as well as for uniform heating, $s_H \gg L$ (Fig. 11, *right panel*). The average deviations between the numerical solutions and analytical approximations are found of the order of $\approx$5%–10% over the logarithmically spaced temperature range of $T > 0.5$ MK.

### 5.5. *Loops with Subsonic Flows*

The hydrostatic solutions calculated here represent solutions of the general magnetohydrodynamic equations (eqs. [1]–[3]) in the limit of no flows, $v(s) = 0$. The solutions for small flow velocities $v(s)$ (compared with the sound speed, $v(s) \ll c_s$), however, are expected to be still close to this asymptotic limit of the hydrostatic case. For slow flows we can therefore take the solutions of the temperature profile $T_e(s)$ and density profile $n_e(s)$ we obtained in the hydrostatic limit, and insert them into the equation of mass conservation (eq. [1]) to obtain the velocity profile $v(s)$,

$$v(s) \approx v_0 \left[\frac{n_0 A_0}{n(s) A(s)}\right] \approx v_0 \frac{T_0 A_0}{T(s) A(s)} \exp\left[\frac{h'(s) - h'(s_0)}{\lambda_p(s)}\right] . \tag{50}$$

This equation tells us that the flow speed has the tendency to increase with height to balance the mass in an exponentially dropping density atmosphere, at least for loops with constant cross section. If the loops are significantly expanding with height, the tendency for accelerated flows goes away. For instance, if the loop expansion is about a factor 2.7 per scale height, the area expansion compensates exactly for the *e*-folding density decrease and siphon flows can exist almost with a constant speed. The sound speed for $T_e = 1.0$ MK is $c_s = 111(\gamma T_{\rm MK})^{1/2}$ km s$^{-1}$ = 111 km s$^{-1}$, with $\gamma = 1$ for an ideal gas (or $\gamma = 5/3$ for an adiabatic gas, respectively). We expect therefore that loops with moderate upflow speeds, of say $v_0 \lesssim 10$ km s$^{-1}$, still fulfil the criterion $v_0 \ll c_s$, and thus can be accurately characterized by our analytical approximations of the hydrostatic solutions.

## 6. DISCUSSION

We have derived accurate analytical approximations of the hydrostatic solutions under the following assumptions: (1) time independent, (2) no flows, and (3) semicircular geometry. The solutions are laid out for uniform or nonuniform heating functions (characterized by an exponential scale length) and account for the vertical variation of solar gravity, for inclined loop planes, and for variable cross sections. Although the real solar corona displays a variety of dynamic processes, hydrostatic solutions are still valid in first order, if mass flows and geometric changes are slow compared with the sound speed. Therefore, the analytic approximations derived here have still a quite accurate validity for coronal structures that have flows and are slowly evolving compared on a hydrodynamic timescale. Also we calculated general corrections for loops with expanding cross sections, which have been calculated previously only for a few special cases (Vesecky et al. 1979; Serio et al. 1981). In the following, we discuss some applications where the analytical approximations may be most useful, the main motivation of this analytical study:

1. *Faster convergence of numerical codes.*—The previously derived scaling laws for loop base pressure $p_0(L, s_H, T_{\rm max})$ and $E_{H0}(L, s_H, T_{\rm max})$ (Serio et al. 1981) involve approximations that cause deviations up to a factor of $\lesssim 5$ from the exact numerical solutions, and thus render the convergence of numerical codes problematic in some parameter regimes, in particular for short heating scale lengths $s_H \ll L$, where numerical convergence is difficult, but which seems to be the most realistic situation for coronal loops. The more accurate scaling laws derived here thus speed up numerical codes significantly in those regimes.

2. *Multithread models of coronal loops.*—Coronal loops seem to consist of unresolved threads even when observed with the highest-resolution instruments down to 1″. The loop threads are likely to be thermally insulated from each other and thus are likely to have independent temperatures. Previous physical modeling of active region loops has been done in the form of single–flux tube concepts (e.g., Landini & Monsignori-Fossi 1975; Craig, McClymont, & Under-

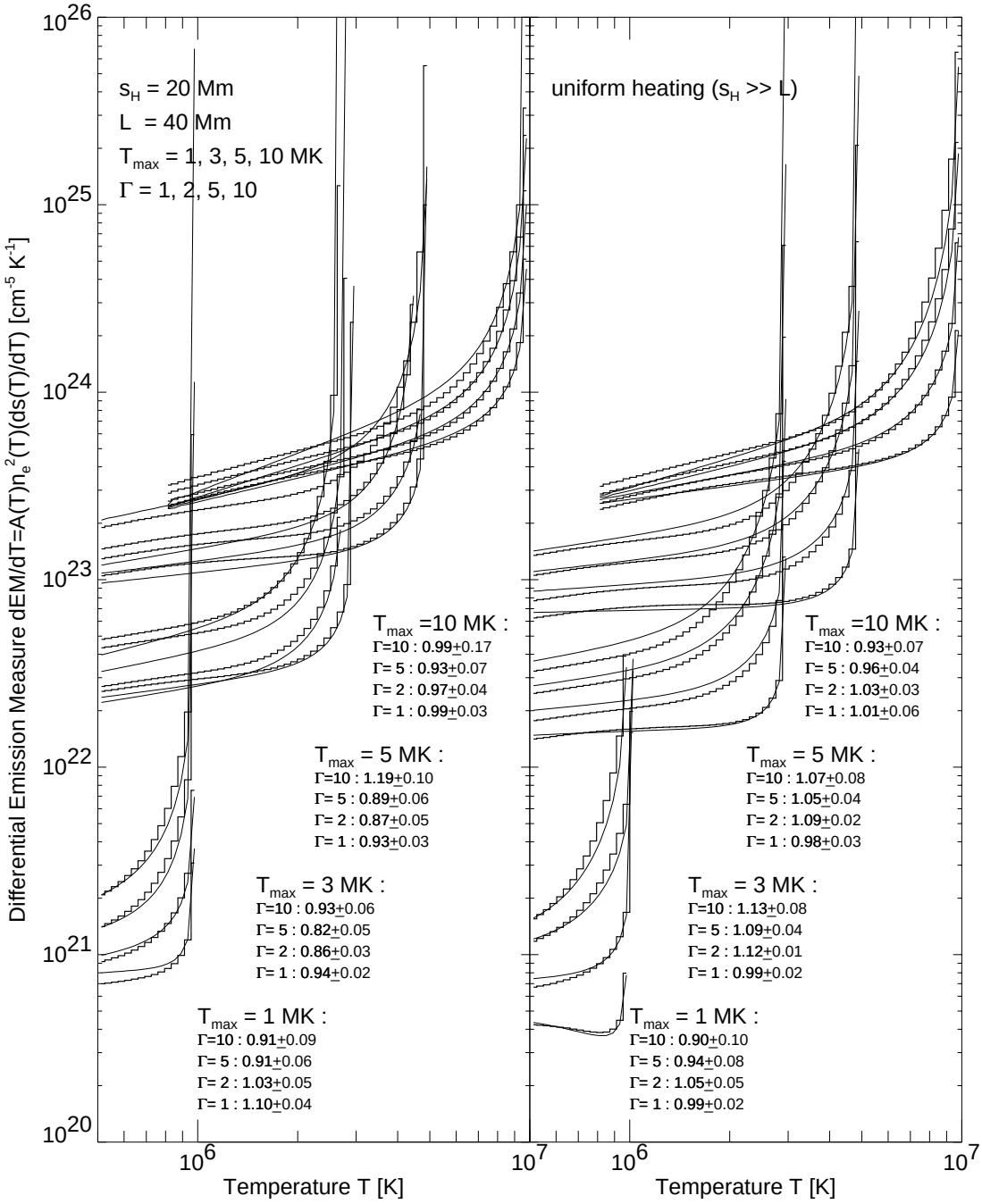


FIG. 11.—Accuracy of differential emission measure (DEM) distributions is shown by comparing the analytical approximations of $dEM(T)/dT_{\rm ana}$ (*smooth curves*) to the numerical solutions $dEM(T)/dT_{num}$ (*histograms*), for a representative subset of numerical solutions in four temperature ranges, four loop expansion factors, and for two different heating scale lengths (i.e., $s_H = 20$ Mm in left panel, and uniform heating in right panel). Note that the average difference is of order 5%–10%.

wood 1978; Rosner et al. 1978; Serio et al. 1981), or in the form of multithread concepts (e.g., Reale & Peres 2000; Aschwanden et al. 2000b). The single–flux tube concept is appropriate for bright loops that can be clearly separated from the background and if they are observed with a narrowband filter, such as with the Extreme-ultraviolet Imaging Telescope (EIT/*SOHO*) (Neupert et al. 1998; Aschwanden et al. 1999, 2000a) or with the *Transition Region and Coronal Explorer* (*TRACE*) (Lenz et al. 1999; Aschwanden et al. 2000b). Single–flux tube modeling, however, is less reliable for faint loops, because the background subtraction (of the coronal background that may have different temperature structure) has much larger uncertainties. Using the analytical approximations derived here, a multithread model of a coronal loop can be parameterized straightforward, using a distribution of base heating rates $N(E_{H0})$ for an ensemble of loop threads, and the synthesized emission measure can be integrated and fitted to the data.

3. *Hydrostatic weighting bias.*—Another severe disadvantage of single–flux tube modeling is the hydrostatic weighting bias (Aschwanden & Nitta 2000), when broad-

band instruments are used, such as the *Yohkoh* Soft X-Ray Telescope (SXT) or the X-Ray Telescope (XRT) on the future Solar-B mission. Such broadband filters with increasing sensitivity with temperature produce a systematic temperature increase with altitude above the limb, because the emission measure-weighted temperature is progressively more sensitive to the longer hydrostatic scale heights $\lambda_T \propto T$ of hotter loop threads (which have their mass distribution systematically spread to higher altitudes). The coronal heating function obtained in single–flux tube models with the *Yohkoh*/SXT instrument (e.g., Priest et al. 2000, MacKay et al. 2000) is therefore subject to confusion with the hydrostatic weighting bias. Using a multithread model where each thread is parameterized with a hydrostatic solution as provided with our analytical approximations, properly accounts for the hydrostatic weighting bias in line-of-sight integrated modeling of EUV and soft X-ray fluxes (Aschwanden 2001).

4. *Coronal heating function.*—The heating function of coronal loops can be determined, in both single–flux tube and multithread models, using a forward-fitting method of our analytical approximations to the observed fluxes seen with different instrumental filters. The heating function is parameterized by the base heating rate $E_{H0}$ and heating scale length $s_H$ as independent parameters in our formulation, which can be varied until the flux model is consistent with the observed SXR or EUV fluxes of coronal structures. A similar approach can be applied to line-of-sight integrated fluxes of the "homogeneous" quiet-Sun corona above the limb, to determine the differential emission measure distribution $dEM(T)/dT$ (Aschwanden & Acton 2001) or statistical averages of quiet-Sun heating functions.

5. *Stellar differential emission measure distributions.*—From stars, we can measure the disk-integrated (differential) emission measure $dEM(T)/dT$ in soft X-rays and EUV, e.g., with *ROSAT, ASCA*, and *Chandra*. On the other side, the global emission from a stellar atmosphere can be modeled by combining the following ingredients: (1) numerical simulation of the surface magnetic field, (2) potential-field extrapolation of the corresponding magnetic field, (3) an ensemble of hydrostatic loops heated by a Pointing flux that is related to the coronal magnetic field, and (4) by integration of the resulting EUV and soft X-ray emission over the entire volume of the stellar coronae to mimic the observed, spatially unresolved $dEM(T)/dT$ of the star. Varying the parameterized heating function from our analytical approximations and fitting them to simulated $dEM(T)/dT$ distributions of stellar data provides then a powerful tool to explore heating mechanisms of stellar coronae (e.g., Schrijver & Aschwanden 2001).

These examples illustrate that the analytical approximations derived in this study have numerous applications in forward-fitting models to solar and stellar coronae, which are too expensive to apply over large parameter spaces by numerical methods. Computer programs in the form of Interactive Data Language (IDL) procedures of the numerical code (§ 3) and the analytical code (Tables 1 and 2) are available from the authors on request. A summary of our analytical approximations (in the sequential order they have to be calculated) is provided in Table 2, with the numerical coefficients given in Table 1.

We thank David Alexander, Giovanni Peres, and Fabio Reale for helpful discussions and Piet Martens for providing numerical routines to calculate temperature profiles with $\beta$-functions. Part of this work was supported by NASA contract NAS5-38099 (*TRACE*), NAS8-00119 (SXT), and NAG5-10832 (LWS).

REFERENCES

Aschwanden, J. J. 2001, ApJ, 559, L171
Aschwanden, M. J., & Acton, L. W. 2001, ApJ, 550, 475
Aschwanden, M. J., Alexander, D., Hurlburt, N., Newmark, J. S., Neupert, W. M., Klimchuk, J. A., & Gary, G. A. 2000a, ApJ, 531, 1129
Aschwanden, M. J., Newmark, J. S., Delaboudiniere, J. P., Neupert, W. M., Klimchuk, J. A., Gary, G. A., Portier-Fornazzi, F., & Zucker, A. 1999, ApJ, 515, 842
Aschwanden, M. J., Nightingale, W., & Alexander, D. 2000b, ApJ, 541, 1059
Aschwanden, M. J., & Nitta, N. 2000, ApJ, 535, L59
Aschwanden, M. J., Schrijver, C. J., & Alexander, D. 2001, ApJ, 550, 1036
Bray, R. J., Cram, L. E., Durrant, C. J., & Loughhead, R. E. 1991, Plasma Loops in the Solar Corona (Cambridge: Cambridge Univ. Press)
Craig, I. J. D., & McClymont, A. N. 1986, ApJ, 307, 367
Craig, I. J. D., McClymont, A. N., & Underwood, J. H. 1978, A&A, 70, 1
Cook, J. W., Cheng, C. C., Jacobs, V. L., & Antiochos, S. K. 1989, ApJ, 338, 1176
Feldman, U. 1992, Phys. Scr., 46, 202
Golub, L., & Pasachoff, J. M. 1997, The Solar Corona (Cambridge: Cambridge Univ. Press)
Klimchuk, J. A., Antiochos, S. K., & Mariska, J. T. 1987, ApJ, 320, 409
Klimchuk, J. A., & Mariska, J. T. 1988, ApJ, 328, 334
Kuin, N. P. M., & Martens, P. C. M. 1982, A&A, 108, L1
Landini, M., & Monsignori-Fossi, B. C. 1975, A&A, 42, 213
Lenz, D. D., DeLuca, E. E., Golub, L., Rosner, R., & Bookbinder, J. A. 1999, ApJ, 517, L155
MacKay, D. H., Galsgaard, K., Priest, E. R., & Foley, C. R. 2000, Sol. Phys., 193, 93
Mariska, J. T., Boris, J. P., Oran, E. S., Young, T. R., Jr., & Doschek, G. A. 1982, ApJ, 255, 783
Martens, P. C. H. 1981, A&A, 102, 156
Martens, P. C. H., Kankelborg, C. C., & Berger, T. E. 2000, ApJ, 537, 471
Meyer, J. P. 1985, ApJS, 57, 173
Neupert, W. M., et al. 1998, Sol. Phys., 183, 305
Parker, E. 1958, ApJ, 128, 669
Peres, G., Orlando, S., Reale, F., & Rosner, R. 2001, ApJ, 563, 1045
Peres, G., Orlando, S., Reale, F., Rosner, R., & Hudson, H. 2000, ApJ, 528, 537
Priest, E. R. 1982, Solar Magnetohydrodynamics (Dordrecht: Reidel)
Priest, E. R., Foley, C. R., Heyvaerts, J., Arber, T. D., MacKay, D., Culhane, J. L., & Acton, L. W. 2000, ApJ, 539, 1002
Reale, F., & Peres, G. 2000, ApJ, 528, L45
Rosner, R., Tucker, W. H., & Vaiana, G. S. 1978, ApJ, 220, 643
Schrijver, C. J., & Aschwanden, M. J. 2002, ApJ, 566, 1147
Serio, S., Peres, G., Vaiana, G. S., Golub, L., & Rosner, R. 1981, ApJ, 243, 288
Tucker, W. H., & Koren, M. 1971, ApJ, 168, 283
Vesecky, J. F., Antiochos, S. K., & Underwood, J. H. 1979, ApJ, 233, 987
Withbroe, G. L. 1988, ApJ, 325, 442